

Plume-ridge interactions: Ridge-ward versus plate-drag plume flow

Fengping Pang¹, Jie Liao^{1,2,3}, Maxim D. Ballmer⁴, Lun Li^{1,2,3}

¹School of Earth Sciences and Engineering, Sun Yat-Sen University, Guangzhou 510275, China

²Guangdong Provincial Key Lab of Geodynamics and Geohazards, Guangzhou 510275, China

³Southern Marine Science and Engineering Guangdong Laboratory (Zhuhai), Zhuhai 519000, China

⁴Department of Earth Sciences, University College London, London, United Kingdom

Correspondence: Jie Liao (liaojie5@mail.sysu.edu.cn)

Abstract

The analysis of mid-ocean ridges and hotspots that are sourced by deep-rooted mantle plumes allows us to get a glimpse of mantle structure and dynamics. Dynamical interaction between ridge and plume processes have been widely proposed and studied, particularly in terms of ridge-ward plume flow. However, the effects of plate drag on plume-lithosphere and plume-ridge interaction remain poorly understood. In particular, the mechanisms that control plume flow towards vs. away from the ridge have not yet been systematically studied. Here, we use 2D thermomechanical numerical models of plume-ridge interaction to systematically explore the effects of (i) ridge spreading rate, (ii) initial plume head radius, and (iii) plume-ridge distance. Our numerical experiments suggest two different geodynamic regimes: (1) plume flow towards the ridge is favored by strong buoyant mantle plumes, slow spreading rates and small plume-ridge distances; (2) plume drag away from the ridge is in turn

21 promoted by fast ridge spreading, at least for small-to-intermediate plumes and large plume-ridge
22 distance. We find that the pressure gradient between the buoyant plume and spreading ridge at first
23 drives ridge-ward flow, but eventually the competition between plate drag and the gravitational force
24 of plume flow along the base of the sloping lithosphere controls the fate of plume (spreading towards
25 vs. away from the ridge). Our results highlight that fast-spreading ridges exert strong plate dragging
26 force, which sheds new light on natural observations of largely absent plume-lithosphere interaction
27 along fast-spreading ridges, such as the East Pacific Rise.

28

29

1 Introduction

Mid-ocean ridges (MORs) and hotspots are two main regions for deep material recycling to the surface of the Earth. However, these two units are not always isolated, but rather show strong interactions in some cases, termed as plume-ridge interaction (Morgan, 1978). Of up to 50 mantle plumes revealed by seismic tomography (French and Romanowicz, 2015; Montelli et al., 2004), more than 20 plumes are found to be associated with nearby ridges (Fig.1a; Ito et al., 2003). Plume-ridge interaction is manifested by geophysical and geochemical anomalies along the ridge axis, e.g., high mantle potential temperature (Dalton et al., 2014), enriched radiogenic isotope anomalies (Cushman et al., 2004; Douglass and Schilling, 1999; Yang et al. 2017), and adjacent lineations of seamounts (Ballmer et al., 2013b; Geissler et al., 2020; L  nat and Merle, 2009). Furthermore, plumes may promote migration of MOR spreading centers (M  ller et al., 1998; Mittelstaedt et al., 2008, 2011; Whittaker et al., 2015), as evidenced by successive ridge jumps towards mantle plumes, e.g., at Iceland, Amsterdam-Saint Paul and Galapagos hotspots (Hardarson et al., 1997; Maia et al., 2011; Mittelstaedt et al., 2012). The interaction dynamics of a ridge with a ridge-centered and off-ridge plume has been widely studied and modeled in analogue and numerical experiments, revealing that the major controlling factors involve the ridge spreading rate, plume buoyancy flux and their spatial distance (Fran  ois et al., 2018; Ito et al., 1997; Kincaid et al., 1996; Ribe et al., 1995; Ribe, 1996; Sleep, 1997). Indeed, most plume-ridge interaction systems are associated with slow-spreading ridges and small mantle plumes and short plume-ridge distances (Fig.1b). However, numerical studies systematically investigating the effects of these parameters on plume-ridge interaction and quantify the controlling forces remain scarce.

51 As has been noted previously, buoyant plumes tend to spread ridge-ward along the sloping base
52 of the lithosphere (Morgan, 1978; Schilling, 1991; Small, 1995). Regions of divergent mantle flow
53 beneath MORs represent the lowest dynamic-pressure regions in the oceanic asthenosphere, and thus
54 tend to suck ambient asthenospheric and plume materials towards the spreading center (Niu, 2014).
55 On the other hand, the viscous drag at the base of the plate tends to convey the spreading plume
56 material away from the MOR (Ribe and Christensen, 1994, 1999). Indeed, plume spreading at the
57 base of the lithosphere is governed by the competition of trench-ward viscous plate drag vs.
58 ridge-ward gravitational and pressure-driven forces (Kincaid et al., 1996). These gravitational and
59 tectonic forces compete with other to control the regime of plume-ridge interaction, but their balance
60 remains to be quantified.

61 The different distribution of hotspots with classified as plume-ridge interaction (ridge-ward
62 spreading) vs. no interaction (plate-drag spreading) also still remains enigmatic. Plume-ridge
63 interaction is much more common near the Mid-Atlantic ridge (MAR) than near the East Pacific Rise
64 (EPR) (Fig. 1a). Near the EPR, only the Pukapuka and Sojourn ridges display clear evidence of
65 ridge-ward flow of the magmatic source, but these volcanic ridges have been attributed to a
66 horizontally viscous differences or small-scale convection in uppermost mantle, and not a mantle
67 plume (Ballmer et al., 2013b; Clouard and Bonneville, 2005; Harmon et al., 2011). A previous study
68 (Jellinek et al., 2003) proposed that fast-spreading ridges guide upwelling mantle flow towards the
69 spreading center to convey the surrounding plumes from deep depth entirely into the MOR melting
70 zone (Fig. 1c), resulting in the absence of hotspots adjacent to the EPR (see also Rowley et al., 2016;
71 Rowley and Forte, 2022). However, fast plate spreading also tends to drag mantle plumes away from
72 the MOR (Kincaid et al., 1995, 1996), leading to the typically parabolic shapes of hotspot swells

73 such as near Hawaii (Ribe and Christensen, 1994). Whether the increased spreading rates in the
74 Pacific vs. Atlantic promote ridge-ward vs. plate-drag plume flow remains an intriguing question.

75 The principal goal of this study is to investigate the process of plume-ridge interaction, with an
76 emphasis on the effects of model parameters on the ridge-ward vs. plate-drag plume spreading. We
77 explore the effects of various model parameters, such as the size of the plume, ridge spreading rate,
78 and plume-ridge distance. Finally, we use our model results to interpret the difference of natural
79 plume-ridge interaction systems in different oceans, particularly the striking difference between the
80 East Pacific and Atlantic in this regard.

81

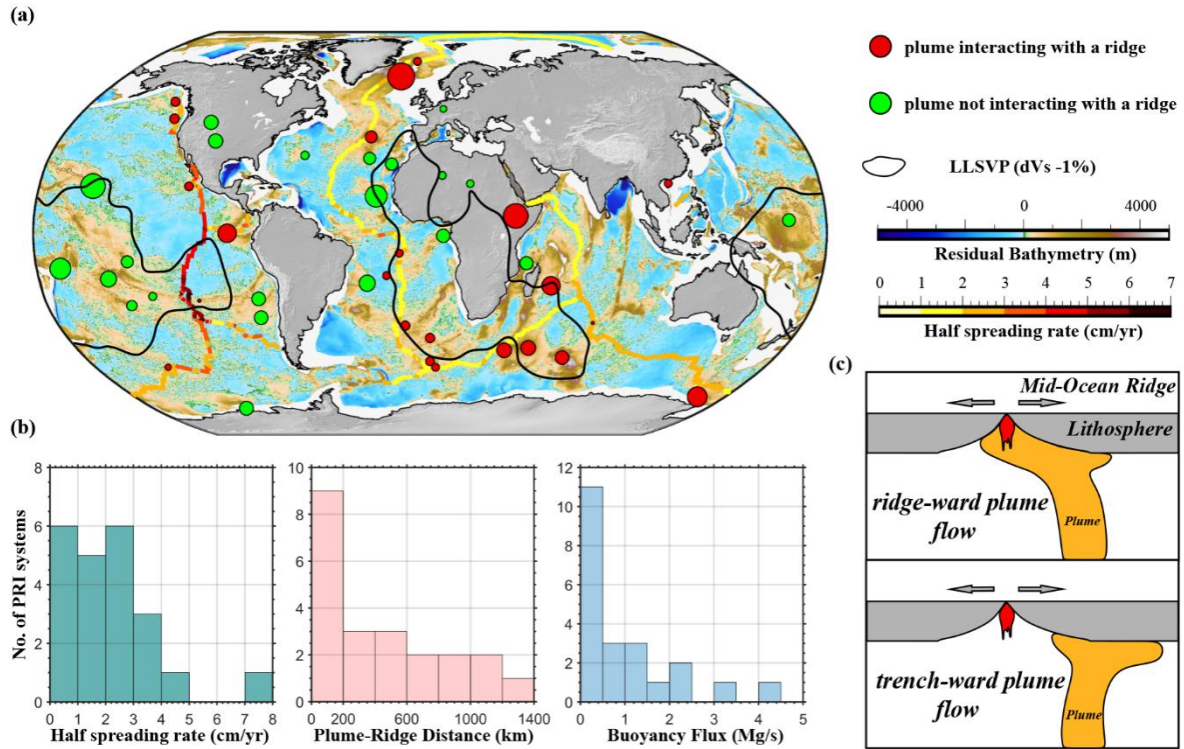


Figure 1. Global plume-ridge interaction systems. **(a)** Global distribution of mid-ocean ridges and mantle plumes. Residual bathymetry of the ocean basins come from Straume et al. (2019). Mid-ocean ridges are painted in color solid lines corresponding to half-spreading rate. Plumes not interacting with a ridge are shown by green circles, and hotspots linked to ridges are in red dots (Ito et al., 2003); size refers to the plume buoyancy flux from Hoggard (2020). Black lines denote the regions of two LLSVPs under the South Africa and Pacific Ocean (Torsvik et al., 2006). **(b)** Histograms of influential factors of plume-ridge interaction systems. Half spreading rate and plume-ridge distance is taken from GPlates (Müller et al., 2016; Whittaker et al., 2015). Plume-ridge interaction systems link to slow-spreading ridge and small mantle plumes and short plume-ridge distance. **(c)** Sketches of ridge-ward (top panel) and plate-drag plume flow (bottom panel) mode proposed, respectively.

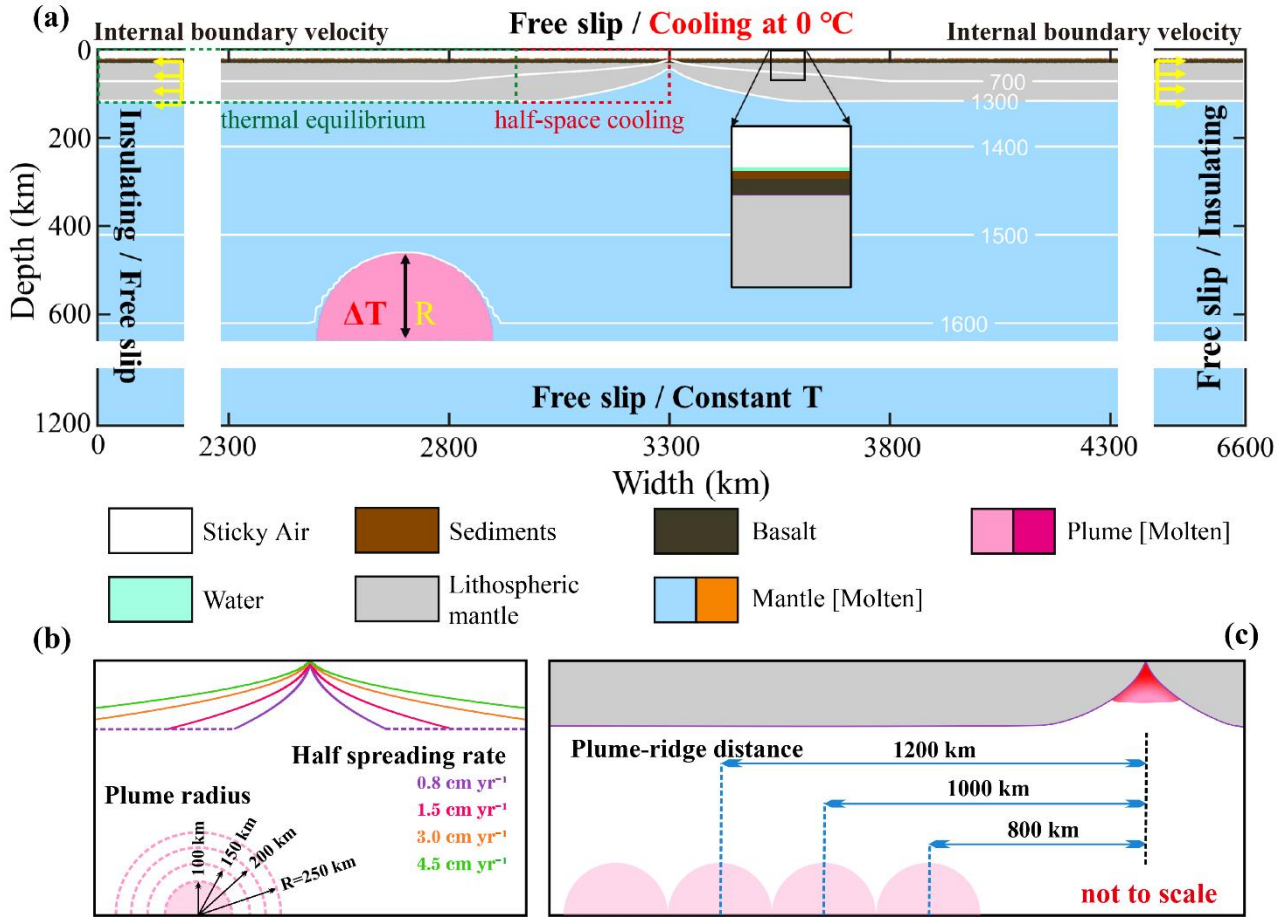


Figure 2. Model setup. **(a)** Initial composition and boundary conditions. The oceanic plate consists of half-space cooling part and the thermal equilibrium part. A 50-Myrs-old mid-ocean ridge sets in the middle of the model based on half-space cooling temperature structure. A thermal and chemical anormal mantle plume locates at 660 km. Different colors indicate the initial rock types and corresponding newly formed molten rock types. Yellow arrows are the half-spreading rates imposed internal in the lithosphere (i.e., from 20 km to 120 km in depth) to simulate ridge spreading. **(b)** Initial tested ridge and plume configurations. **(c)** Initial tested plume-ridge distances.

2 Numerical modelling

2.1 Modelling methods

To explore plume-lithosphere and plume-ridge interaction, we conduct numerical simulations

utilizing the 2D thermo-mechanical code I2VIS, which is based on staggered finite difference method combined with marker-in-cell techniques (Gerya and Yuen, 2003, 2007). This modeling framework uses both Eulerian grids and randomly-distributed Lagrangian markers to jointly solve equations of conservation of mass, momentum and energy (Eq. (1)-(3), respectively):

$$\nabla \cdot \vec{v} = 0 \quad (1)$$

$$\frac{\partial \sigma'_{ij}}{\partial x_j} - \frac{\partial P}{\partial x_i} + \rho g_i = 0 \quad (2)$$

$$\rho C_p \left(\frac{DT}{Dt} \right) = -\nabla \cdot \vec{q} + H_r + H_a + H_s + H_l \quad (3)$$

where v refers to the velocity, σ'_{ij} the deviatoric stress tensor, P the pressure, ρ the density, g the gravity acceleration, $\frac{D}{Dt}$ the Lagrangian time derivative, C_p the heat capacity, and q the heat flux. Additionally, H_r , H_a , H_s , and H_l are the radioactive, adiabatic, shear, and latent heat productions, respectively.

We employ a non-Newtonian visco-plastic rheology (Gerya and Yuen, 2007) in the models. The viscous rheology depends on stress, temperature and pressure. The appropriate viscosity is expressed as that of a composite diffusion and dislocation-creep material (Eq. (4)).

$$\frac{1}{\eta_{vis}} = \frac{1}{\eta_{diff}} + \frac{1}{\eta_{disl}} \quad (4)$$

in which η_{diff} and η_{disl} are the diffusion and dislocation creep viscosity, respectively, and can be further computed as Eq. (5) and Eq. (6):

$$\eta_{diff} = \frac{1}{2} A \sigma_{crit}^{1-n} \exp \left(\frac{PV_a + E_a}{RT} \right) \quad (5)$$

$$\eta_{disl} = \frac{1}{2} A^n \dot{\epsilon}_{II}^{\frac{1-n}{n}} \exp \left(\frac{PV_a + E_a}{nRT} \right) \quad (6)$$

where P is the pressure, T is the temperature, $\dot{\epsilon}_{II}$ is the second invariant of the strain rate tensor, σ_{crit} is the diffusion-dislocation creep transition stress, and A , E_a , V_a , and n are the strain rate pre-exponential factor, activation energy, activation volume, and stress exponent, respectively. The

128 plastic behavior η_{pla} is described by the Drucker-Prager yield criterion (Byerlee, 1978; Ranalli,
129 1995) according to Eq. (7) and Eq. (8):

$$130 \quad \sigma_y = C + P\varphi \quad (7)$$

$$131 \quad \eta_{pla} = \frac{\sigma_y}{2\dot{\epsilon}_{II}} \quad (8)$$

132 in which σ_y is the yield stress, C is the rock cohesion and φ is the effective friction coefficient.
133 The effective viscosity η_{eff} of rocks is thus constrained by both viscous and plastic deformation,
134 where the rheological behavior depends on the minimum viscosity attained between ductile and
135 brittle fields:

$$136 \quad \eta_{eff} = \min(\eta_{vis}, \eta_{pla}) \quad (9)$$

137 Partial melting, melt extraction and percolation are also considered in the model in a simplified
138 way (Gerya, 2013). The melt fraction (M_0) of the crust are assumed to increase with temperature and
139 are calculated according to Eq. (10):

$$140 \quad M_0 = 0 \text{ when } T \leq T_{solidus}$$

$$141 \quad M_0 = \frac{(T - T_{solidus})}{(T_{liquidus} - T_{solidus})} \quad \text{when } T_{solidus} < T < T_{liquidus} \quad (10)$$

$$142 \quad M_0 = 1 \text{ when } T \geq T_{liquidus}$$

143 where $T_{solidus}$ and $T_{liquidus}$ are the solidus and liquidus temperature of different rock types,
144 respectively, taken from Katz et al. (2003).

145 In our model, melt extraction is modeled indirectly and considered as an instantaneous process
146 (Gerya et al., 2015). The extracted melt is assumed to move vertically from the molten source and
147 then added to the bottom of the crust. Partial melt is extracted from the mantle and instantaneously
148 displaced to the bottom of the crust and converted into hot mafic magma, obeying the conservation
149 of material. The amount of extracted melt during the evolution of each experiment is traced by the

150 Lagrangian markers (Gerya, 2013). The total amount of melt, M , for every marker excludes the
 151 amount of previously extracted melt according to Eq. (11):

$$152 \quad M = M_0 - \Sigma_n M_{ext} \quad (11)$$

153 where $\Sigma_n M_{ext}$ refers to the total melt fraction extracted during the previous n melt extraction
 154 timesteps.

155 The effective density of mafic magma and molten crust depends on its melt fraction and is
 156 calculated as (Gerya et al., 2015; Gülcher et al., 2020):

$$157 \quad \rho_{eff} = \rho_{solid}(1 - M + M \frac{\rho_{0,molten}}{\rho_{0,solid}}) \quad (12)$$

158 where $\rho_{0,molten}$ and $\rho_{0,solid}$ are the reference densities of the molten and solid crust. ρ_{solid} is the
 159 crust density at given pressure and temperature, which can be computed as:

$$160 \quad \rho_{solid} = \rho_{0,solid}[1 - \alpha(T - 298)][1 + \beta(P - 0.1)] \quad (13)$$

161 with thermal expansion $\alpha = 3 \times 10^{-5} K^{-1}$ and compressibility $\beta = 10^{-11} Pa^{-1}$.

162 Surface processes, such as erosion and sedimentation, are considered by solving the transport
 163 equation on the Eulerian nodes at each time step (Gerya and Yuen, 2003). Our erosion/sedimentation
 164 model uses gross-scale erosion/sedimentation rates which are independent of local elevation and
 165 topography (Burov and Cloetingh, 1997). We use constant and moderate rates of erosion (0.315
 166 mm/yr) and sedimentation (0.0315 mm/yr), respectively, which falls within naturally observed
 167 ranges.

168

169 **2.2 Model setup**

170 The size of the model box is 6600×1200 km, with a nonuniform grid of 501×301
 171 computational nodes in length and depth, respectively (Fig. 2). The densest grid is located in the

center of the model domain (i.e., grid size decreases linearly from 20 km at the edges to 2 km at the ridge axis), where plume-ridge interaction would happen. The model consists of a 20 km thick sticky air layer to accommodate crustal surface deformation. To reproduce the oceanic lithosphere, we choose a typical layered model, where the crust is composed of a water level (2 km), a sediment layer (1.5 km), and a basalt layer (7.5 km). The oceanic lithosphere and asthenosphere in the model are both modeled as dry olivine (the different colors for the mantle lithosphere and asthenosphere in the figures of this paper are only for better visualization). Besides, a 50-Myrs-old mid-ocean ridge is set on central part of the lithosphere, splitting the model domain into two parts. At the depth of 660 km, a 200-km-wide semicircular plume is located on the left of model domain, corresponding to the onset of plume-ridge interaction from the mantle transition zone. Detailed rock parameters are listed in Table 1.

The thermal conditions at the top and bottom boundaries are fixed at 273 and 2513 K, respectively. The left and right boundaries are both insulating, with no external heat flow across them. The initial temperature structure of the mantle is adiabatic (0.5 K km^{-1}), which results in a temperature at 660 km depth of 1843 K. The initial temperature structure of the oceanic plate consists of half-space cooling part and thermal equilibrium part (Fig. 2a). The half-space cooling model is used to describe the oceanic plate younger than 50 Myr, and the thermal equilibrium structure is used to describe older oceanic parts. In other words, the thermal age of the lithosphere far away from the ridge is fixed at 50 Myr with a constant plate thickness (i.e., $\sim 100 \text{ km}$). The hot plume is set a circular thermal and compositional (see Table 1) anomaly with an excess temperature of 250 K to trigger a rising thermochemical plume. All the velocity boundaries are free slip boundaries. Additional internal boundary velocities are imposed at 500 km from each side boundary in the

lithosphere to maintain the imposed half spreading rate (Fig. 2a).

Table 1. Rock physical properties used in the numerical models.

Parameters	Sediments	Ocean Crust	Mantle	Plume	Reference ^a
Flow law	Wet quartz	Basalt	Dry olivine	Wet olivine	
Preexponential factor $A(\text{Pa}^n\text{s})$	1.97×10^{17}	4.80×10^{22}	3.98×10^{16}	5.01×10^{20}	1
Activation energy $E_a(\text{KJ mol}^{-1})$	154	238	532	470	1
Activation volume $V_a(\text{J bar}^{-1}\text{mol}^{-1})$	0	0	1	0.8	1
Exponent n	2.3	3.2	3.5	4	1
Cohesion $C(\text{Pa})$	2×10^7	2×10^7	2×10^7	2×10^7	1
Effective friction coefficient ϕ	0.6/0.3	0.6/0.3	0.6/0.3	0.6/0.3	1
Density $\rho(\text{Kg m}^{-3})$	2600	3000	3300	3270	2
Radioactive heating $H_r(\text{W m}^{-3})$	2×10^{-6}	2.2×10^{-7}	2.2×10^{-8}	2.5×10^{-8}	2

a: 1-(Ranalli, 1995), 2-(Turcotte and Schubert, 2014)

Other physical parameters used for all rocks include: gas constant $R=8.314 \text{ J K}^{-1}\text{mol}^{-1}$, thermal expansion $\alpha=3 \times 10^{-5} \text{ K}^{-1}$, compressibility $\beta=1 \times 10^{-11} \text{ Pa}^{-1}$, heat capacity $C_p=1000 \text{ J kg}^{-1}\text{K}^{-1}$.

3 Model Results

We conduct a series of numerical experiments to investigate ridge suction versus plate drag acts on plumes. The effects of three major model parameters (i.e., the spreading rate of mid-ocean ridge, the initial plume head radius, and the plume-ridge distance) are systematically studied. The typical dynamic evolution of models with ridge-ward vs. plate-drag plume flow are demonstrated.

3.1 Model evolution with ridge-ward plume flow

For models with dominant ridge-ward flow, the typical model evolution is shown in Fig. 3 (the major model parameters used in this case are: the half spreading rate of 8 mm yr^{-1} , the initial plume

209 head radius of 200 km, and the off-axis distance of 800 km). In the early plume head stage, the
210 buoyant mantle plume rises up rapidly in a mushroom-like shape (Fig. 3b) and imposes dynamic
211 stresses at the base of the overriding oceanic plate, leading to significant surface uplift (Fig. 3a). The
212 ascending plume experiences extensive decompression melting at the base of the overriding plate,
213 and due to the dynamic overpressure, spreads laterally, forming two branches that flow in opposite
214 directions (Fig. 3c). A large amount of plume material is eventually entrained towards the spreading
215 center, ponding underneath the ridge axis, and significantly affecting the ridge dynamics. The
216 entrainment of hot plume material promotes decompression melting (Figs. 3d, e) and increases the
217 temperature beneath the ridge (Fig. S2). Within the overlying lithosphere, the buoyant mantle plume
218 leads to stress localization and strongly weakens the oceanic plate (Figs. S1, S3). As the plume
219 eventually flows upward along the increasingly sloping base of the plate near the MOR, melting and
220 crust production occurs (Fig. S1), forming an oceanic plateau of thickened crust. In addition to this
221 gravitational force that guides plume material of the right branch ridge-ward, plate spreading drags
222 both branches in the opposite direction. Moreover, convective and tectonic stresses (“plume push”
223 and “ridge suction”) affect both branches of the plume in a different way. As a consequence, the two
224 branches evolve asymmetrically: the right branch that flows towards the ridge axis is more vigorous
225 than the left branch, and the plume tail is also tilted towards the spreading center (Figs. 3c-e). For a
226 more detailed discussion of the underling controlling forces, see below.

227

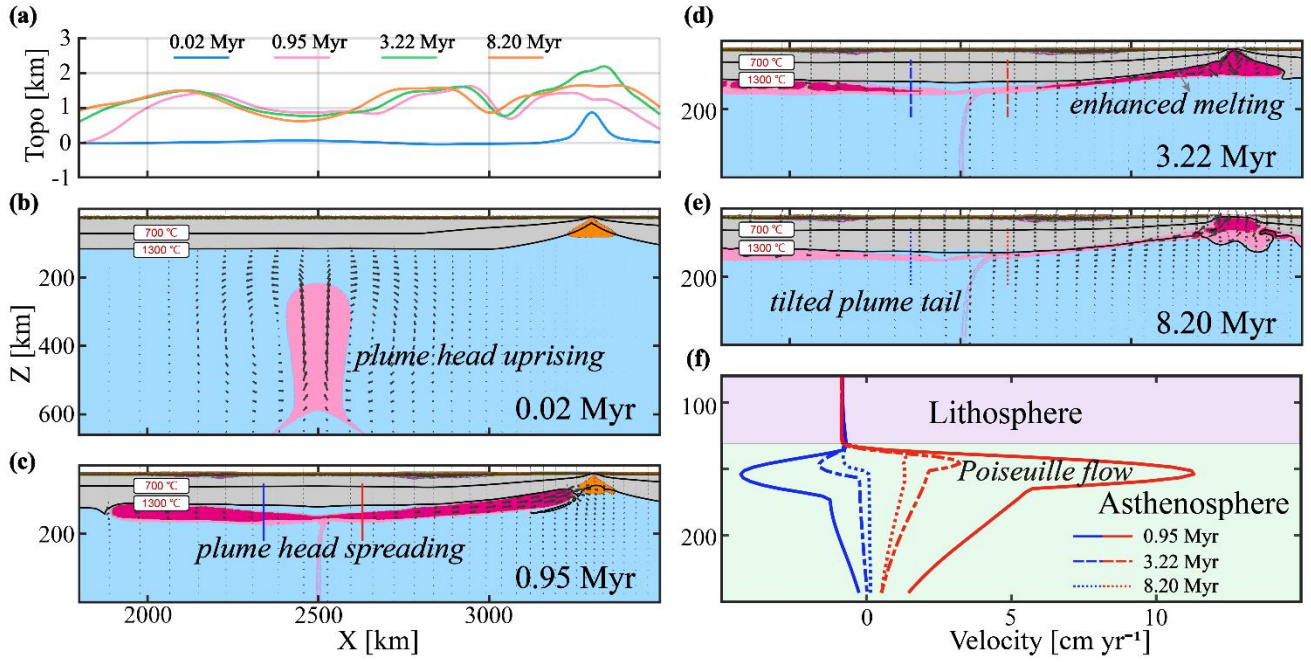


Figure 3. The evolution of the reference model M12 (see Table S1 in supplementary material) with dominant ridge-ward plume flow. The main model parameters employed in this case are: half spreading rate of 8 mm yr⁻¹, an initial plume head radius of 200 km, and an off-axis distance of 800 km. **(a)** surface topography over time along the flow path. **(b-e)** Snapshots of composition for the reference model (M12). **(f)** Profiles of the horizontal velocity component over time at the sections as indicated (color-coded) in panel (c-e).

The mantle flow horizontal velocity profiles (Fig. 3f) further demonstrate the dominance of ridge-ward plume flow, showing that plume flow is faster towards the spreading ridge than away from it. The velocity profiles elucidate dominant Poiseuille flow, with the maximum flow velocities in the middle of the asthenospheric channel. Such velocity profiles are well consistent with observations of seismic anisotropy at the Reunion plume (Barruol et al. 2019). The branches of the spreading plume head move significantly faster than the overriding plate. Therefore, plate drag actually slows down the spreading of the plume branches in this model case. Because of the

asymmetrical spreading of the plume head, the buoyancy flux carried by the right branch of the plume (density anomaly multiplied by horizontal velocity from Figure 3f) is also much larger than that carried by the left branch.

3.2 Model evolution with plate-drag plume flow

For models with dominant plume flow away from the ridge (“plate-drag flow”), the typical model evolution is shown in Fig. 4. The controlling parameters of the representative model shown in Figure 4 are the same as for the model shown in Figure 3, except for a smaller radius (100 km) and faster spreading ridge (half spreading rate: 45 mm yr⁻¹). At first, the ascending plume head spreads out similarly as in the case described above and interacts with the overriding oceanic lithosphere. The largest surface uplift is sustained just above the plume head (Fig. 4a), slightly different from the previous model in which the highest surface elevation is observed on both sides of the plume conduit (Fig. 3a). Related to this spreading and uplift, divergent stresses are sustained in the overlying lithosphere (Fig. S4), but no weakening or yielding occurs (Fig. S6). The plume head undergoes significant decompression melting near the deflection point (Fig. 4c). However, thick and cold lithosphere prevents magma from extracting (Fig. S4). As the plume cools, partially molten plume gets solidified speedily (Figs. 4d-e and S5). In contrast to the reference model from section 3.1, this model displays most plume material flowing away from the ridge, likely due to dominant plate drag (Figs. 4c-e). Indeed, the left branch of the plume consistently displays larger buoyancy fluxes and maximum velocities than the right side over time (Fig. 4f).

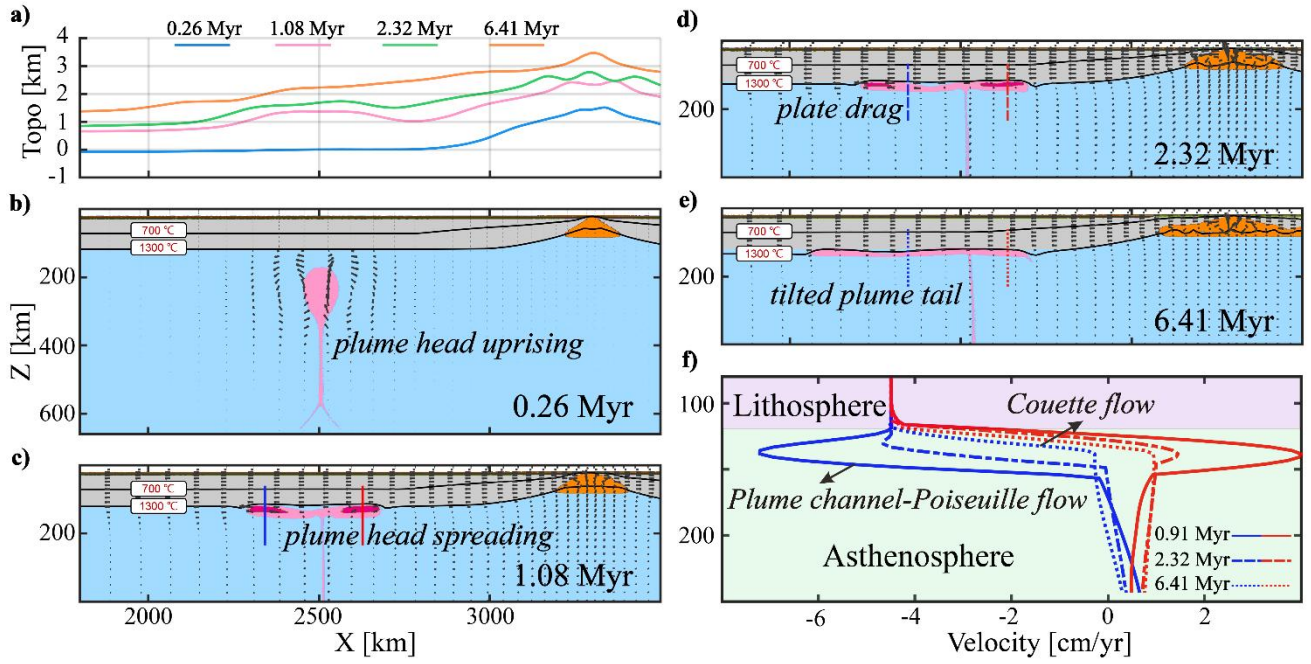


Figure 4. Same as Figure 3 for case M77 (i.e., the reference model for the plate-drag plume flow regime). The main model parameters employed in this case are: half spreading rate of 45 mm yr^{-1} , an initial plume head radius of 100 km, and an off-axis distance of 800 km.

The underlying mechanism for dominant plate-drag plume flow is the frictional shear force of the moving plate, which is further demonstrated by the plume flow velocity profiles (Fig. 4f). In the early plume head stage ($\sim 1.08 \text{ Myr}$), the plume spreads out faster than plate velocity, which is primarily driven by the overpressure of the ponding plume head at this stage. After a short amount of time ($\sim 2.32 \text{ Myr}$), however, plume spreading becomes significantly slower than plate velocity, and hence plate drag drives and controls the plume flow. Indeed, the flow mode in the asthenosphere rapidly shifts from Poiseuille flow (i.e., active plume flow) to Couette flow (i.e., passive plume flow) (Fig. 4f), indicating the increasing role of plate drag on plume flow, soon after an initial of plume-head spreading.

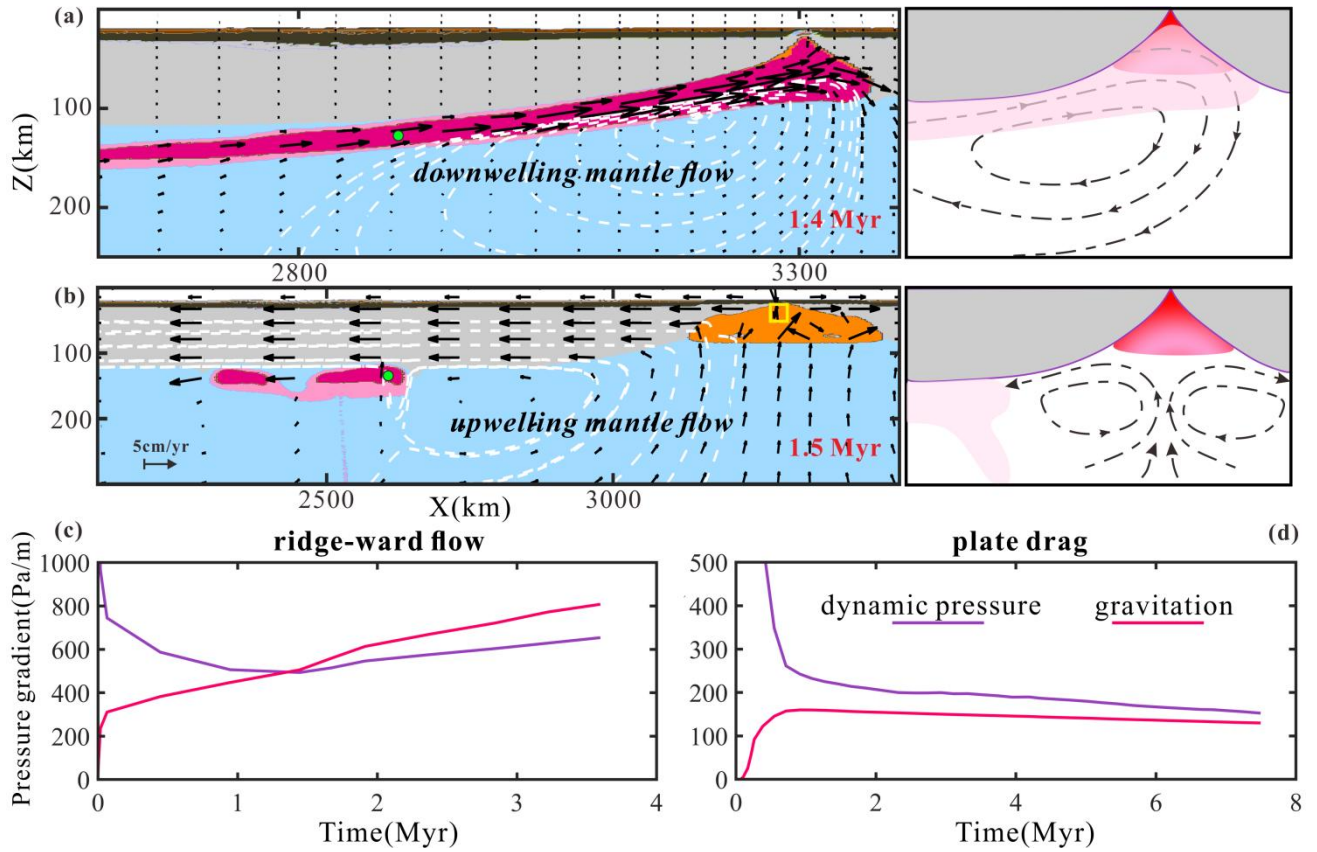


Figure 5. Comparison between models with ridge-ward vs. plate-drag plume flow. **(a)** Ridge-ward flow with downwelling beneath the MOR (results from case M12 as in Figure 3). White dashed lines are streamlines; black arrows visualize the flow field. Schematic of flow in the sub-panel on the right-hand side. **(b)** Plate-drag flow with upwelling mantle corner flow beneath the MOR (results from case M77 as in Figure 4). **(c)** The dynamic pressure and gravitational gradient of plume marker (i.e. green circle in (a)) over time. The yellow box in (b) marks the location for the computation of average dynamic pressure at the ridge, needed for the calculation of the dynamic pressure gradient (see text). **(d)** The dynamic pressure and gravitational gradient of plume marker (i.e. green circle in (b)) over time.

3.3 Two modes of plume-lithosphere interaction

291 The dominant ridge-ward and dominant plate-drag plume flow regimes are two distinct modes of
 292 plume-plate interaction. The differences between these two regimes are further demonstrated in
 293 terms of mantle flow (Figs. 5a,b), driving forces (Figs. 5c,d).

294 In the ridge-ward dominated models, clockwise mantle develops from the plume to the spreading
 295 ridge (Fig. 5a). Molten plume material flows to the spreading ridge and occupies the space
 296 underneath the ridge axis, sustaining significant asymmetry of mid-ocean ridge melting (Conder et
 297 al., 2002). As a consequence to the continuous supply of the plume material, downward mantle flow
 298 forms beneath the ridge axis. This flow pattern dramatically differs from that shown in the plate-drag
 299 dominated models, which show upward mantle flow underneath the ridge axis (Fig. 5b), as typical
 300 for the flow beneath a MOR without the influence of a plume.

301 The distinct modes of plume-ridge interaction (ridge-ward vs. plate-drag flow) are controlled by
 302 the competition of the tectonic (plate drag, ridge suction) and gravitational (plume buoyancy) driving
 303 forces. On one hand, the moving plate drags sub-lithospheric plume material away from the ridge.
 304 On the other hand, the mechanism of ridge-ward flow is twofold. First, the buoyant plume material
 305 flows along the sloping base of the lithosphere towards the shallow ridge along the gravitational
 306 gradient. Second, the plume is driven along the dynamic-pressure gradient from the pressure
 307 maximum (e.g., where the plume sustains dynamic topograph) towards the pressure minimum
 308 beneath the diverging ridge. These gravitational (G_{gv}) and pressure-driven (G_{dp}) gradients are
 309 calculated by tracing plume markers (Figs. 5c,d) as follows:

$$310 \quad G_{dp} = (P_{mk} - P_r)/L \quad (12)$$

$$311 \quad G_{gv} = (\rho_0 - \rho_{mk}) * g * k \quad (13)$$

312 where P_{mk} is the dynamic pressure of plume marker and P_r is the averaged pressure in a 50 km box
313 at ridge center (Fig. 5b); L is the horizontal distance from plume marker to ridge axis; ρ_{mk} and ρ_0
314 are the plume marker density and initial density, respectively; g is the gravitational acceleration; k is
315 the local slope of the base of the lithosphere.

316 In the early stage of model evolution, the plume head's dynamic overpressure is dominant,
317 driving plume spreading in both directions (Fig. 5c), in particular in the direction of the low-pressure
318 ridge. However, this pressure gradient systematically diminishes over time as the plume (head)
319 spreads. Once the spreading plume approaches the ridge, the lithospheric slope increases. At some
320 point, the gravitational gradient exceeds the dynamic pressure gradient, taking over as the major
321 driving force of guiding plume material towards the ridge. Consequently, one of the essential
322 conditions for plume-ridge interaction is that the plume must be able to reach the critical zone near
323 the ridge, where the slope is sufficiently steep to take over for the ever diminishing pressure gradient.
324 This implies that the plume buoyancy must (1) overcome the shearing force of plate drag, and (2) the
325 pressure-gradient must be sustained long enough to reach the critical zone, in which the gravitational
326 gradient can take over. The (1) shearing force scales with the rate of ridge spreading, and the (2)
327 critical zone is more readily reached for high buoyancy fluxes at a given plume-ridge distance.

328

329

330 **3.4 Influence of model parameters**

331 We have systematically investigated the effect of the three main model parameters (i.e., the
332 spreading rate of the mid-ocean ridge, initial plume head radius and plume-ridge distance) on
333 plume-ridge interaction. We explored half spreading rates of the ridge of 8, 15, 30, and 45 mm yr⁻¹,

334 corresponding to ultra-slow, slow, medium, and fast-spreading mid-ocean ridges, respectively (Gerya,
335 2012). We varied initial plume head radii in the range of 100 km to 300 km. Further, we tested
336 plume-ridge distance in the range of 600 to 1400 km.

337 **3.4.1 Plume head radius**

338 The size of the buoyant plume exerts an important control on plume-ridge interaction. Small
339 plumes tend to be dragged away from the ridge, with typically larger lateral fluxes of the left branch
340 than the right branch of the spreading plume (Figs. 6a,b). The buoyancy flux in each branch is
341 calculated by multiplying the velocity of the markers in plume pipe (Figs. 6d-f) by the density. The
342 dynamic pressure decreases with decreasing plume size (Fig. S8a), and the pressures gradient is thus
343 not strong enough for small plumes to reach the ridge. Plate shearing dominates plume flow soon
344 after plume head spreading, and the moving plate then drags plume head material, leaving a tilted
345 plume tail (Fig. 6d). In contrast, with larger initial plume head radius or buoyancy flux, the ponding
346 plume spreads more vigorously (Fig. 6c) and sustains much higher overpressures at the base of the
347 plate (Fig. S8a). This vigorous spreading can overcome plate drag to drive Poiseuille flow in both
348 directions. Once the right plume branch approaches the spreading center, it is attracted and further
349 accelerated by ridge suction. The plume tail is also markedly tilted towards the ridge axis due to
350 asymmetric spreading (Fig. 6f). The larger the plume is, the more plume material gets entrained by
351 the spreading center.

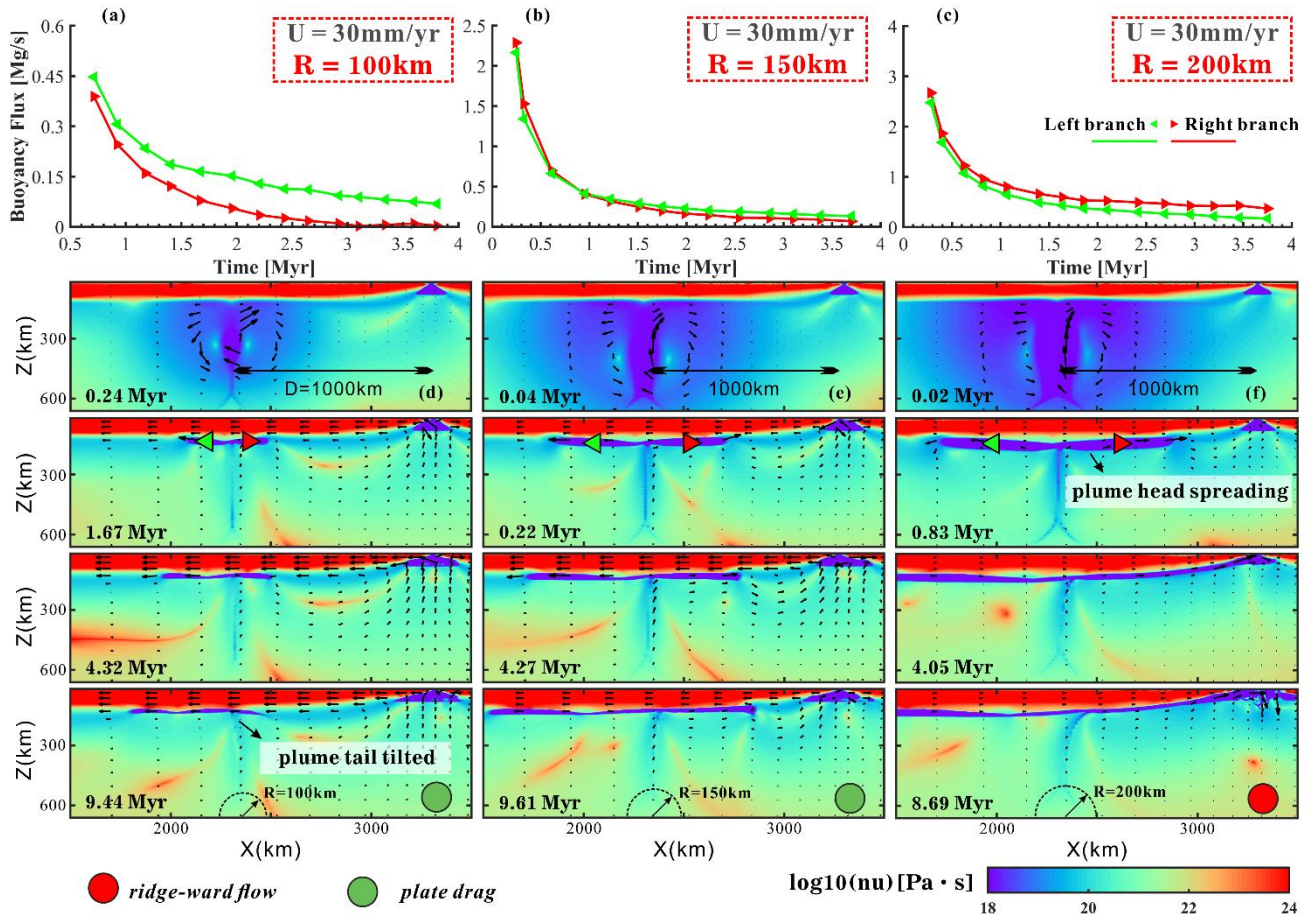
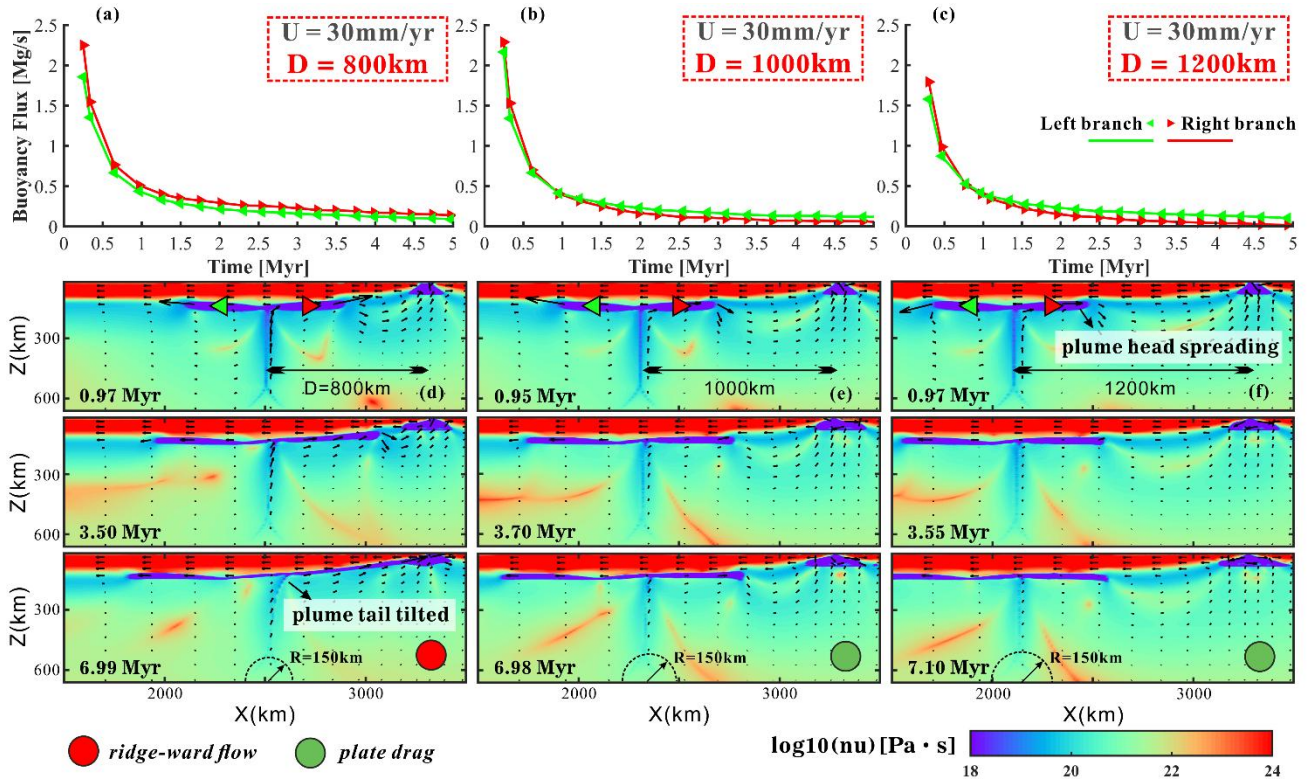


Figure 6 Models varying initial plume head radii (model M53, M58, and M63, Table S1 in supplementary material) shown by buoyancy flux and viscosity. **(a-c)** Buoyancy flux in spreading plume branches over time. Green and red triangles are markers used for buoyancy flux calculation. **(d-f)** Viscosity snapshots of models with different plume head radii. Models with green circle represent plate-drag plume flow and ridge-ward plume flow in red.

3.4.2 Plume-ridge distance

Plume-ridge distance also controls the regime of plume-ridge interaction. A plume at large distances spreads similarly as a plume at a small distance, but is less likely to get affected by ridge suction (Figs. 7e,f). The pressure gradient between the plume and ridge drives the ridge-ward plume flow. However, the larger the plume-ridge distance, the smaller the pressure gradient would be (Fig.

364 S8b), resulting in a lower buoyancy flux across the plume pipe (Figs. 7a-c). In the cases of distant
 365 plumes, the spreading of the plume head is strongly affected by plate drag (Figs. 7b, c). On the other
 366 hand, the difficulty in sustaining ridge-ward plume flow may also link to the heat transfer between
 367 the cold plate and the hot plume rocks. With gradually cooling from upper plate by heat conduction
 368 and diffusion, the viscosity of plume increases as it cools. Such increasing viscosity slows the plume
 369 down, stopping the ridge-ward plume flow eventually (Figs. 7e, f). Hence, for cases with large
 370 plume-ridge distances and hence travel times, the ponding plume head cools and is ultimately carried
 371 away by the moving plate.



372 **Figure 7.** Models varying plume-ridge distances (model M57-M59, Table S1 in supplementary
 373 material) shown by buoyancy flux and viscosity. (a-c) Buoyancy flux in spreading plume branches
 374 over time. Green and red triangles are markers used for buoyancy flux calculation. (d-f) Viscosity
 375 snapshots of models with different plume-ridge distances. Models with green circle represent
 376 plate-drag plume flow and ridge-ward plume flow in red.

378

379 **3.4.3 Half spreading rate of ridge**

380 Another parameter that is worth investigating is the spreading rate of the ridge. The modeling
 381 results indicate that fast-spreading ridges promote plume flow away from the ridge due to the friction
 382 (Figs.8 and 9a). With increasing spreading rate, the effect of plate shearing on plume-lithosphere
 383 interaction increases, as quantified by the spreading fraction. The spreading fraction γ (Eq.(14)) is
 384 defined here as the ratio of ridge-ward vs. plate-drag plume volume fluxes. We integrated the
 385 ridge-ward plume volume flux (right branch), V_{rw} , and plate-drag plume volume flux (left branch),
 386 V_{tw} . V_p is the total plume volume flux in the model. Ridge-ward plume spreading is dominant for
 387 positive γ ; plate-drag plume spreading is dominant for negative γ .

$$388 \quad \gamma = (V_{rw} - V_{tw})/V_p \quad (14)$$

389 In the early stage (~ 1 Myr), pressure-driven flow dominates in all models and spreading
 390 fractions are positive, mainly driven by the expansion of the overpressured plume heads along the
 391 pressure gradient. After a certain time, the spreading fractions decrease dramatically with the decay
 392 of the mantle plume activity, representing the transition from the ridge-ward to the plate-drag regime
 393 in some cases. The characteristic spreading fractions after 8 Myr model time as a function of our
 394 model parameters are shown in Fig. 8. This compilation of our results reveals that the dominance of
 395 ridge-ward flow decreases with increasing spreading rate and off-axis distance, but significantly
 396 increases with plume size. For models with fast-spreading ridges, the parameter range of plate-drag
 397 flow dominated models is expanded, indicating the critical role of plate drag in restricting ridge-ward
 398 flow and plume-ridge interaction.

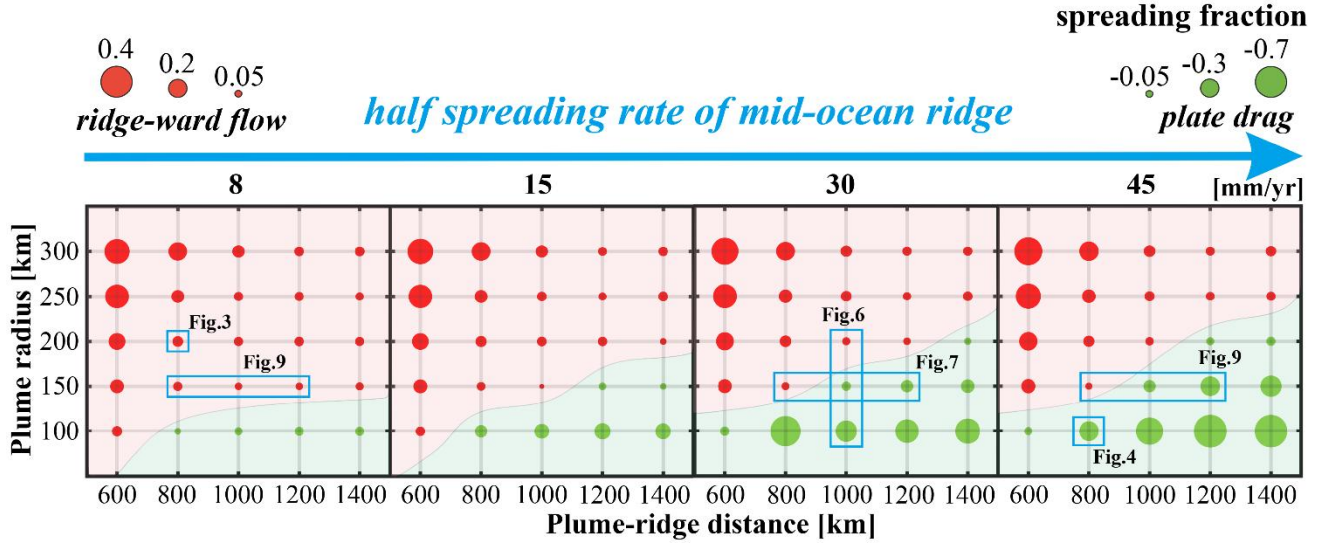


Figure 8. Parameter regime diagram of the contrasting modes of plume-ridge interaction. Spreading fractions γ (Eq. (14)) at ~ 8 Myr model time. Each of the circles represents one of the numerical experiments, and sizes refer to γ . Circles in red and green represent models with dominant ridge-ward plume flow and plate drag, respectively.

The transition from ridge-ward (positive γ) to plate-drag (negative γ) flow in some of our cases is mainly determined by the competition between the effects of pressure-driven plume head spreading and plate shearing. The overpressure in the plume head drives plume materials towards the lower pressure spreading center, while the moving plate shears plume away. Hence, we quantify the shear force of the overriding oceanic plate on the plume head using an integral approach:

$$F_s = \int \sigma_{xz} dA \quad (15)$$

Equation (15) is employed to calculate the shear force, where F_s is the total shear force the spreading oceanic plate exerts on the uppermost part of the plume. σ_{xz} is the shear stress on each mantle plume grid cell, A refers to the area of each grid cell. The pressure gradients, both

gravitational and dynamic pressure, are calculated by tracing the plume markers according to equations (12-13). As the plume material rises to the base of the lithosphere, the shear force exerted by the plate increases over time. We find that the integrated shear force between the spreading plate and the plume increases significantly as half spreading rate increases (Fig. 9c).

Conversely, ridge spreading rates control gravitational and pressure-driven plume driving forces (Fig. 9d). Increasing the spreading rate of the ridge implies a smaller dynamic pressure gradient, because the pressure gradient is related to the plate thickness difference at the ridge and plume, which is dependent on the spreading rate. A fast-spreading ridge also implies a smaller gravitational gradient, because it leaves a more shallowly-dipping lithospheric base. Thus, relatively strong plate shearing combined with relatively small pressure and gravitational gradients tend to advance plate-drag plume flow for high spreading rates.

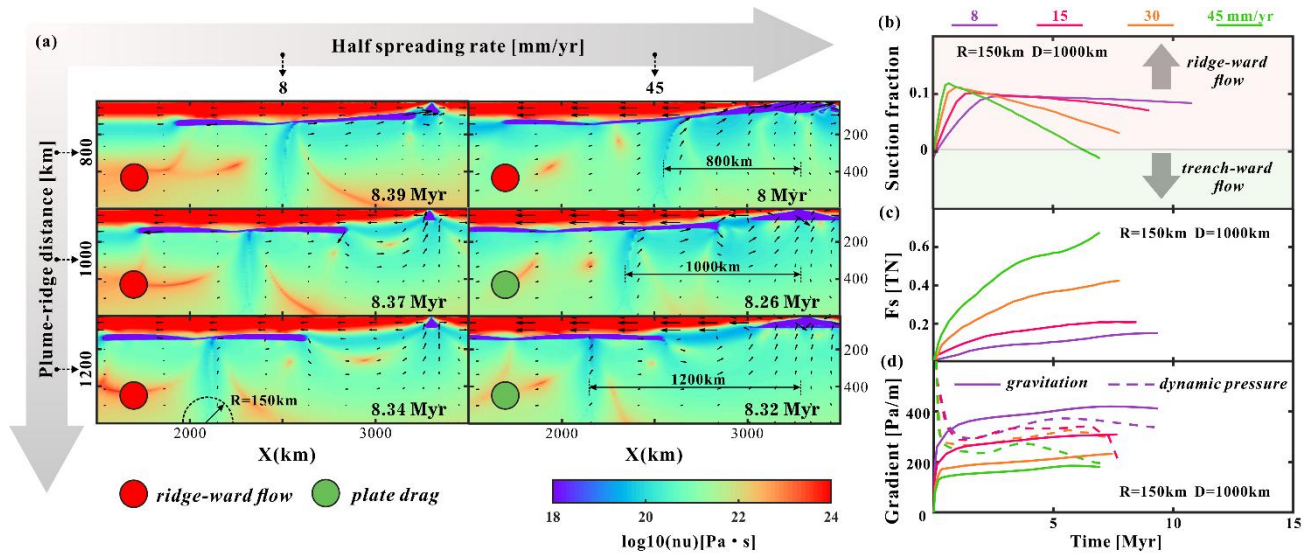


Figure 9. Model results influenced by different half spreading rates. **(a)** Effect of spreading rate on ridge-ward flow vs. plate-drag flow. Viscosity snapshots are shown (model M7-M9, M82-M84, Table S1 in supplementary material). Fast-spreading ridge promotes plume material dragged. Models with green circle represent plate-drag plume flow and ridge-ward plume flow in red. **(b)** Dynamic

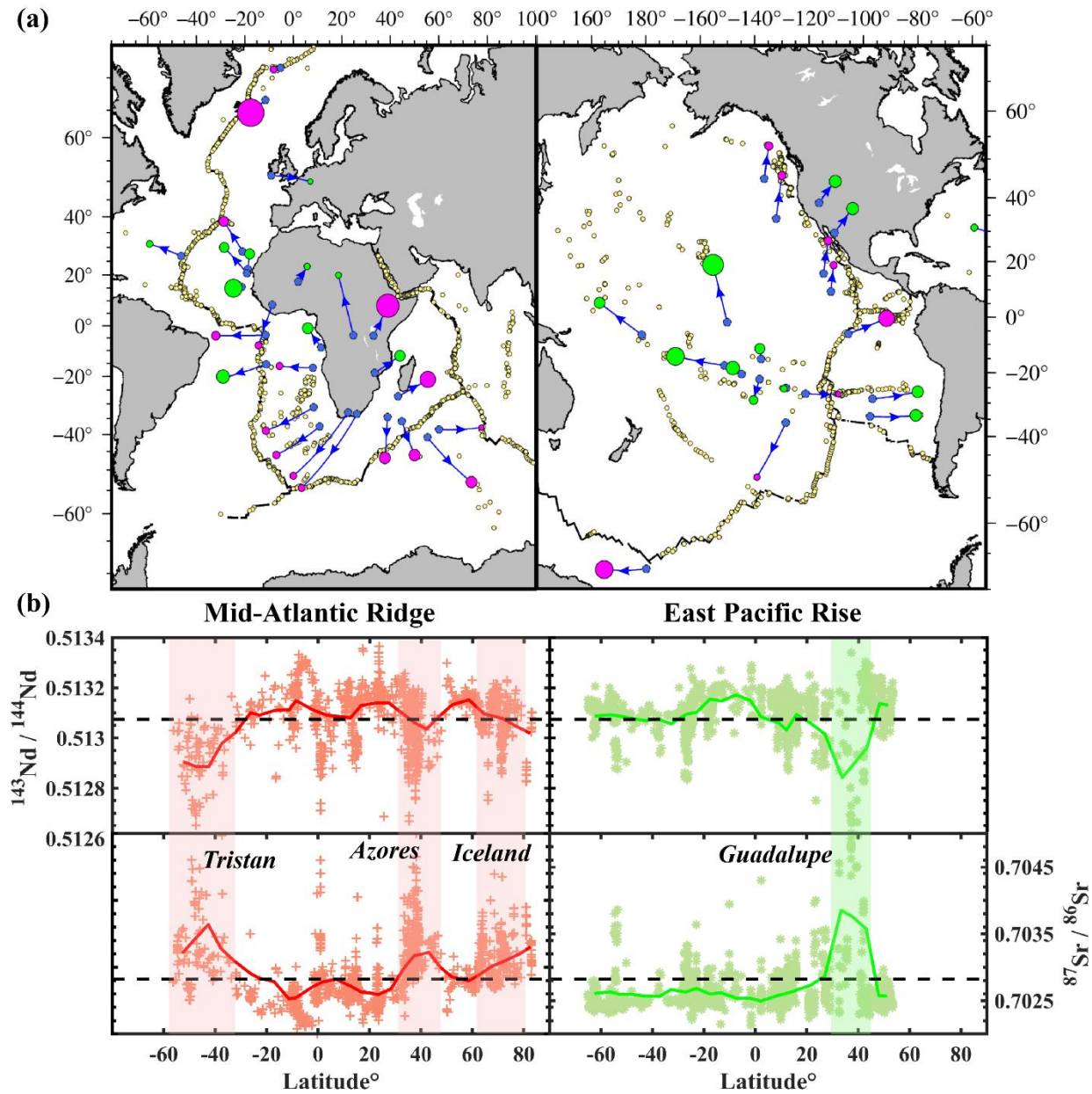
evolutions of ridge-ward and plate-drag plume flow, revealed by defined ridge spreading fraction (eq.14). **(c)** Shear force (F_s) between moving plate and plume material under different spreading rates. **(d)** Pressure gradient between plume head and ridge center in different half spreading rate models. The solid and dash lines are the plume gravitation and dynamic pressure gradient, respectively.

4 Discussion

Natural observations show that there are only very few hotspots indicative of ridge-ward plume flow close to the East Pacific Rise (EPR) (Fig. 10a), in contrast to many such hotspots in the Atlantic and Indian oceans. A previous study (Jellinek et al., 2003) proposed that fast-spreading ridges such as the EPR efficiently convey any surrounding plumes into the spreading center from the deep mantle (Fig. 1c), which leads to fewer hotspots nearby fast-spreading ridges. However, based on our modeling results, fast-spreading ridges tend to promote plate-drag flow of the spreading plume material, providing an alternative explanation to the relatively absence of hotspots along the EPR. We discuss the viability of this potential explanation by comparing with geological and geophysical observations (Fig. 10).

Firstly, the plate drag effect of fast-spreading ridges on plumes is evidenced by geophysical observations. We locate the positions of the mantle plumes at the core-mantle boundary (CMB) and the associated hot spots on the surface based on global seismic tomography (Jackson et al., 2021; Koppers et al., 2021). A lateral offset between the deep and surface positions of plumes is a common feature, indicating the deflection of plumes due to mantle flow. Specifically, a large portion of

453 plumes located in the Atlantic are tilted towards the mid-ocean ridge. However, only very few
 454 plumes in the Pacific are tilted towards the mid-ocean ridge; indeed, the majority of plumes are tilted
 455 away from the ridges, indicating the significant effect of plate drag on plumes beneath fast plates.
 456 Such observations are consistent with the predictions of our models with dominant plate-drag plume
 457 spreading.



458
 459 **Figure 10.** A compilation of hotspots along with spreading ridges in the Atlantic and the Pacific. (a)
 460 Distribution of surface hotspots (circles) together with depth-projected source locations at CMB

(blue dots) of the plumes based on (Jackson et al., 2021). Plumes in magenta circles are mantle plumes interacted with ridges (Ito et al., 2003), and plumes not interacted with ridges are shown as green circles, whose size refers to the plume buoyancy flux (Hoggard et al., 2020). Yellow dots are MORB samples mapped in (b). **(b)** Plot of radioactive isotopes ratios along ridge MORB samples. The data are downloaded from the PetDB Database (<http://portal.earthchem.org/>). The colored symbols refer to samples in different mid-ocean ridge. Main hotspots influencing MORBs are labeled with shaded bands. The black dash lines are the mean MORB isotopes ratio from Gale (2013). Red and green lines are the mean ratios of the samples in Mid-Atlantic ridge and EPR, respectively.

Geochemical studies suggest that mantle plumes are enriched in light rare earth elements (LREEs) and radiogenic isotopes of Sr and Pb but depleted in Nd isotopes. These geochemical anomalies are evident in MORB at the sites of active plume-ridge interaction (Cushman et al., 2004; Douglass and Schilling, 1999; Yang et al. 2017). We find that MORB sampled along both the Mid-Atlantic ridge and the EPR indeed display geochemical anomalies (Fig. 10b), indicating ridge-ward flow of plume material at specific locations. However, the Mid-Atlantic MORB dataset is slightly more heterogeneous than the East Pacific Rise in terms of geochemical isotopes. The EPR is basically characterized as normal oceanic basalt, along which only very few regions show composition associated with nearby plumes. This contradicts the view (Jellinek et al., 2003) that mantle plumes are fully entrained into the central MOR melting zone at fast-spreading ridges.

Based on our modeling results, initial plume head radius and plume-ridge distance also control the mode of plume-ridge interaction. However, there is only a small difference in terms of the fraction of interacting vs. non-interacting plumes for different buoyancy fluxes B : a small majority of

major plumes (5 of 8 with $B > 1.6$ Mg/s) vs. a small minority of small-to-intermediate plumes (11 of 25 for $B < 1.6$ Mg/s) display interaction with the ridge (Fig. 11a). The underlying cause for this observation remains unclear, but may be related to the distribution of large plumes globally with many of them being located very far from MORs. Also note that our 2D models are limited in that plume material cannot spread in the out-of-plane direction, hence somewhat exaggerating the effects of buoyancy flux. In any case, the distribution of observed plume buoyancy fluxes (Hoggard et al., 2020) varies little across different oceans (Fig. 11a). Therefore, the effects of plume size are not a good candidate to explain the notable difference between the Atlantic and Pacific in terms of plume-ridge interaction mode.

On the other hand, compared with the Atlantic and Indian Oceans, Pacific plumes are located significantly further from the mid-ocean ridge (Fig. 11b). Plume-ridge distances in the Pacific are mostly >2000 km, which exceeds the maximum plume-ridge interaction distance of 1400 km (Schilling, 1991). Most plumes in the Pacific exhibit the typical signatures of plume flow away from the ridge, such as parabolic swell shapes (e.g., Society, Marquesas and Hawaii plumes; Ballmer et al., 2013a; Ballmer et al., 2015; Cheng et al., 2015; Wolfe et al., 2009), and linear volcanic chains (Buff et al., 2021; Clouard and Bonneville, 2005; Jackson et al., 2010). Age-progressive hotspots trails indicate an absence of dominant ridge-ward flow. By contrast, most plumes in the Atlantic have been close to the ridge since the opening of the ocean. These mantle plumes (e.g., Discovery, Iceland, Tristan-Gough; O'Connor et al., 2012) did not move much since the breakup of the Atlantic. One factor may be that the underlying plume generation zone (i.e., the edge of the African LLSVP) round largely parallel to the Mid-Atlantic Ridge (Fig. 1) (Torsvik et al., 2006). In this case, plume-ridge distance may play a critical role in the plume-ridge interaction, and could explain the striking

505 difference between the Pacific and Atlantic in terms of the number of plume-ridge interacting vs.
 506 non-interacting systems. In addition, the rapid movement of the Pacific plate tends to inhibit
 507 ridge-ward plume flow at a given plume-ridge distance. The distribution of interacting (stars) vs
 508 non-interacting systems in Figure 11b is almost exactly as predicted by our models for the coupled
 509 effects of plume-ridge distance and plate velocity. For example, we note that fast-spreading ridges
 510 can still interact with adjacent plumes under the appropriate conditions. In the case of very short
 511 plume-ridge distances, there is good evidence of plume-ridge interaction in the southern Pacific
 512 ocean (e.g., Louisville plume; Conder et al., 2002; Toomey et al., 2002; Vlastélic and Dosso, 2005).
 513 Based on a series of numerical modeling as well as geological and geophysical observations, we
 514 conclude that mantle plumes in the Pacific are more likely to spread away from the ridge and into the
 515 direction of plate motion than in the Atlantic and Indian Oceans. The tendency of fast plate velocities
 516 to promote plume spreading away from the MOR through viscous drag may depend, however, on the
 517 details of lithosphere-asthenosphere rheological coupling such as the presence of a weak decoupling
 518 (e.g., melt) layer (Rychert et al., 2020). Further studies of plume spreading and plume-ridge
 519 interaction are needed to shed light on the coupling of the plate-mantle system.

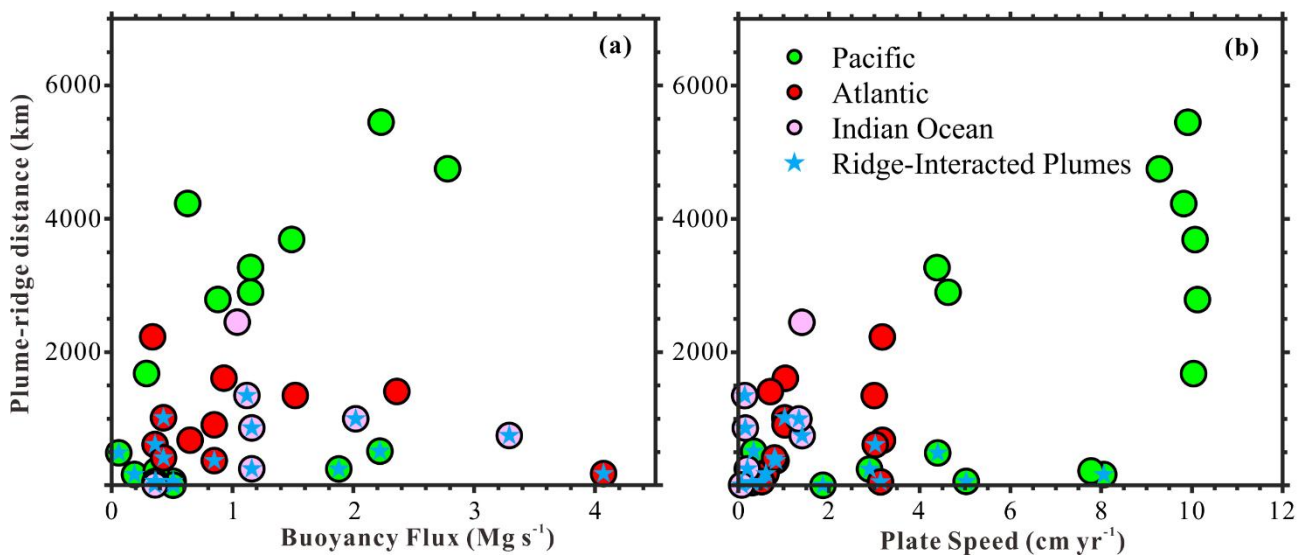


Figure 11. Buoyancy flux, plate speed and plume-ridge distance of mantle plumes in different oceans. Mantle plumes in the Pacific, Atlantic and Indian Ocean are shown in green, red and pink circles, respectively. Blue stars marked the ridge-interacted plumes according to Ito et al. (2003). **(a)** Plot of plume-ridge distance and plume buoyancy flux. Data are from Hoggard et al. (2020). **(b)** Plot of plume-ridge distance and plate speed at the location of plumes. Plume-ridge distance come from GPlates (Müller et al., 2016; Whittaker et al., 2015), and plate speed data come from Becker et al. (2015)

5 Conclusion

In this study, we explore the evolution of plume-ridge interaction with 2D thermomechanical numerical models. Based on model results, we find that:

- (1) Plume-ridge interaction is mainly governed by the competition between the effects of plume spreading (overpressure in the plume-head stage), upward gravitationally-driven flow of the plume along the base of the sloping lithosphere and plate shearing. These driving forces are controlled by plume size, plume-ridge distance and the spreading rate of the mid-ocean ridge.
- (2) MOR spreading does not only draw upwelling plumes into the spreading center, but also tends to drag mantle plumes away from the ridge. Plume flow away from the ridge is favored by small and/or distant plumes as well as fast spreading rates, whereas plume flow towards the ridge is promoted by large and/or nearby plumes, as well as slow spreading rates.
- (3) Considering the high plate velocity and typically large plume-ridge distances, mantle plumes in the Pacific are more likely to be dragged away from the EPR than being drawn towards the ridge center.

543

544

545 **Code availability**

546 The source numerical modeling code in this study is available from the corresponding author upon
547 reasonable request.

548

549 **Data availability**

550 The data that support the findings of this study are available from the corresponding author upon
551 reasonable request.

552

553 **Author contribution**

554 Fengping Pang performed all numerical models, interpreted results and wrote the manuscript. Jie
555 Liao proposed the study, modify the code and contributed to rewriting and scientific discussion.
556 Maxim D. Ballmer contributed with significant help in rewriting and scientific discussion. Lun Li
557 participated in discussion and interpretations. All authors have read and edited draft versions of the
558 paper and have approved the final version.

559

560 **Competing interest**

561 The authors declare that they have no conflict of interest.

562

563 **Acknowledgement**

564 This research is financially supported by NSFC projects (U1901214, 41974104, 91855208) and
565 Guangdong project 2017ZT07Z066. We are grateful to Prof. Taras Gerya for his long-lasting
566 guidance on our geodynamical modeling. We gratefully acknowledge Hongjian Fang for insightful

567 discussions. Numerical simulations were performed on the clusters of National Supercomputer
568 Center in Guangzhou (Tianhe-II).
569

Reference

- Ballmer, M. D., Ito, G., Wolfe, C. J. and Solomon, S. C.: Double layering of a thermochemical plume in the upper mantle beneath Hawaii, *Earth Planet. Sci. Lett.*, 376, 155–164, doi:10.1016/j.epsl.2013.06.022, 2013a.
- Ballmer, M. D., Conrad, C. P., Smith, E. I. and Harmon, N.: Non-hotspot volcano chains produced by migration of shear-driven upwelling toward the East Pacific Rise, *Geology*, 41(4), 479–482, doi:10.1130/G33804.1, 2013b.
- Ballmer, M. D., Ito, G. and Cheng, C.: Asymmetric dynamical behavior of thermochemical plumes and implications for hawaiian lava composition, *Geophys. Monogr. Ser.*, 208, 35–57, doi:10.1002/9781118872079.ch3, 2015.
- Barruol, G., Sigloch, K., Scholz, J. R., Mazzullo, A., Stutzmann, E., Montagner, J. P., Kiselev, S., Fontaine, F. R., Michon, L., Deplus, C. and Dymant, J.: Large-scale flow of Indian Ocean asthenosphere driven by Réunion plume, *Nat. Geosci.*, 12(12), 1043–1049, doi:10.1038/s41561-019-0479-3, 2019.
- Becker, T. W., Schaeffer, A. J., Lebedev, S. and Conrad, C. P.: Toward a generalized plate motion reference frame, *Geophys. Res. Lett.*, 42(9), 3188–3196, doi:10.1002/2015GL063695, 2015.
- Buff, L., Jackson, M. G., Konrad, K., Konter, J. G., Bizimis, M., Price, A., Rose-Koga, E. F., Blusztajn, J., Koppers, A. A. P. and Herrera, S.: “Missing Links” for the Long-lived Macdonald and Arago Hotspots, South Pacific Ocean, *Geology*, 49(5), 541–544, doi:10.1130/G48276.1, 2021.
- Burov, E. and Cloetingh, S.: Erosion and rift dynamics: New thermomechanical aspects of post-rift evolution of extensional basins, *Earth Planet. Sci. Lett.*, 150(1–2), 7–26, doi:10.1016/s0012-821x(97)00069-1, 1997.

592 Byerlee, J.: Friction of rocks, *Pure Appl. Geophys. PAGEOPH*, 116(4–5), 615–626,
 593 doi:10.1007/BF00876528, 1978.

594 Cheng, C., Allen, R. M., Porritt, R. W. and Ballmer, M. D.: Seismic constraints on a double-layered
 595 asymmetric whole-mantle plume beneath Hawai'i, *Hawaiian Volcanoes From Source to Surf.*, 19–34,
 596 doi:10.1002/9781118872079.ch2, 2015.

597 Clouard, V. and Bonneville, A.: Ages of seamounts, islands, and plateaus on the Pacific plate, *Spec.*
 598 *Pap. Geol. Soc. Am.*, 388, 71–90, doi:10.1130/0-8137-2388-4.71, 2005.

599 Conder, J. A., Forsyth, D. W. and Parmentier, E. M.: Asthenospheric flow and asymmetry of the East
 600 Pacific Rise, MELT area, *J. Geophys. Res. Solid Earth*, 107(B12), ETG 8-1-ETG 8-13,
 601 doi:10.1029/2001jb000807, 2002.

602 Cushman, B., Sinton, J., Ito, G. and Dixon, J. E.: Glass compositions, plume-ridge interaction, and
 603 hydrous melting along the Galapagos spreading center, 90.5 °W to 98 ° W, *Geochemistry, Geophys.*
 604 *Geosystems*, 5(8), doi:10.1029/2004GC000709, 2004.

605 Dalton, C. A., Langmuir, C. H. and Gale, A.: Geophysical and geochemical evidence for deep
 606 temperature variations beneath mid-ocean ridges, *Science* (80-.), 344(6179), 80–83,
 607 doi:10.1126/science.1249466, 2014.

608 Douglass, J., Schilling, J. G. and Fontignie, D.: Plume-ridge interactions of the Discovery and Shona
 609 mantle plumes with the southern Mid-Atlantic Ridge (40°-55° S), *J. Geophys. Res. Solid Earth*,
 610 104(B2), 2941–2962, doi:10.1029/98jb02642, 1999.

611 François, T., Koptev, A., Cloetingh, S., Burov, E. and Gerya, T.: Plume-lithosphere interactions in
 612 rifted margin tectonic settings: Inferences from thermo-mechanical modelling, *Tectonophysics*,
 613 746(October 2015), 138–154, doi:10.1016/j.tecto.2017.11.027, 2018.

614 French, S. W. and Romanowicz, B.: Broad plumes rooted at the base of the Earth's mantle beneath
615 major hotspots, *Nature*, 525(7567), 95–99, doi:10.1038/nature14876, 2015.

616 Gale, A., Dalton, C. A., Langmuir, C. H., Su, Y. and Schilling, J. G.: The mean composition of ocean
617 ridge basalts, *Geochemistry, Geophys. Geosystems*, 14(3), 489–518, doi:10.1029/2012GC004334,
618 2013.

619 Geissler, W. H., Wintersteller, P., Maia, M., Strack, A., Kammann, J., Eagles, G., Jegen, M.,
620 Schloemer, A. and Jokat, W.: Seafloor evidence for pre-shield volcanism above the Tristan da Cunha
621 mantle plume, *Nat. Commun.*, (2020), doi:10.1038/s41467-020-18361-4, 2020.

622 Gerya, T.: Origin and models of oceanic transform faults, *Tectonophysics*, 522–523, 34–54,
623 doi:10.1016/j.tecto.2011.07.006, 2012.

624 Gerya, T. V.: Three-dimensional thermomechanical modeling of oceanic spreading initiation and
625 evolution, *Phys. Earth Planet. Inter.*, 214, 35–52, doi:10.1016/j.pepi.2012.10.007, 2013.

626 Gerya, T. V. and Yuen, D. A.: Characteristics-based marker-in-cell method with conservative
627 finite-differences schemes for modeling geological flows with strongly variable transport properties,
628 *Phys. Earth Planet. Inter.*, 140(4), 293–318, doi:10.1016/j.pepi.2003.09.006, 2003.

629 Gerya, T. V. and Yuen, D. A.: Robust characteristics method for modelling multiphase
630 visco-elasto-plastic thermo-mechanical problems, *Phys. Earth Planet. Inter.*, 163(1–4), 83–105,
631 doi:10.1016/j.pepi.2007.04.015, 2007.

632 Gerya, T. V., Stern, R. J., Baes, M., Sobolev, S. V. and Whattam, S. A.: Plate tectonics on the Earth
633 triggered by plume-induced subduction initiation, *Nature*, 527(7577), 221–225,
634 doi:10.1038/nature15752, 2015.

635 Gülcher, A. J. P., Gerya, T. V., Montési, L. G. J. and Munch, J.: Corona structures driven by

636 plume–lithosphere interactions and evidence for ongoing plume activity on Venus, *Nat. Geosci.*,
637 13(8), 547–554, doi:10.1038/s41561-020-0606-1, 2020.

638 Hardarson, B. S., Fitton, J. G., Ellam, R. M. and Pringle, M. S.: Rift relocation - A geochemical and
639 geochronological investigation of a palaeo-rift in northwest Iceland, *Earth Planet. Sci. Lett.*,
640 153(3–4), 181–196, doi:10.1016/s0012-821x(97)00145-3, 1997.

641 Harmon, N., Forsyth, D. W., Weeraratne, D. S., Yang, Y. and Webb, S. C.: Mantle heterogeneity and
642 off axis volcanism on young Pacific lithosphere, *Earth Planet. Sci. Lett.*, 311(3–4), 306–315,
643 doi:10.1016/j.epsl.2011.09.038, 2011.

644 Hoggard, M. J., Parnell-turner, R. and White, N.: Hotspots and mantle plumes revisited: Towards
645 reconciling the mantle heat transfer discrepancy, *Earth Planet. Sci. Lett.*, 542, 116317,
646 doi:10.1016/j.epsl.2020.116317, 2020.

647 Ito, G., Lin, J. and Gable, C. W.: Interaction of mantle plumes and migrating mid-ocean ridges:
648 Implications for the Galapagos plume-ridge system, , v, 1–3, 1997.

649 Ito, G., Lin, J. and Graham, D.: Observational and theoretical studies of the dynamics of mantle
650 plume-mid-ocean ridge interaction, *Rev. Geophys.*, 41(4), doi:10.1029/2002RG000117, 2003.

651 Jackson, M. G., Hart, S. R., Konter, J. G., Koppers, A. A. P., Staudigel, H., Kurz, M. D., Blusztajn, J.
652 and Sinton, J. M.: Samoan hot spot track on a “hot spot highway”: Implications for mantle plumes
653 and a deep Samoan mantle source, *Geochemistry, Geophys. Geosystems*, 11(12),
654 doi:10.1029/2010GC003232, 2010.

655 Jackson, M. G., Becker, T. W. and Steinberger, B.: Spatial Characteristics of Recycled and
656 Primordial Reservoirs in the Deep Mantle, *Geochemistry, Geophys. Geosystems*, 22(3),
657 doi:10.1029/2020GC009525, 2021.

658 Jellinek, A. M., Gonnermann, H. M. and Richards, M. A.: Plume capture by divergent plate motions:
 659 Implications for the distribution of hotspots, geochemistry of mid-ocean ridge basalts, and estimates
 660 of the heat flux at the core-mantle boundary, *Earth Planet. Sci. Lett.*, 205(3–4), 361–378,
 661 doi:10.1016/S0012-821X(02)01070-1, 2003.

662 Jiang, Q., Jourdan, F., Olierook, H. K. H., Merle, R. E. and Whittaker, J. M.: Longest continuously
 663 erupting large igneous province driven by plume-ridge interaction, *Geology*, 1–3,
 664 doi:10.1130/G47850.1, 2020.

665 Kincaid, C., Ito, G. and Gable, C.: Laboratory investigation of the interaction of off-axis mantle
 666 plumes and spreading centres, *Nature*, 376(6543), 758–761, doi:10.1038/376758a0, 1995.

667 Kincaid, C., Schilling, J.-G. and Gable, C.: The dynamics of off-axis plume-ridge interaction in the
 668 uppermost mantle, *Earth Planet. Sci. Lett.*, 137(1–4), 29–43, doi:10.1016/0012-821X(95)00201-M,
 669 1996.

670 Koppers, A. A. P., Becker, T. W., Jackson, M. G., Konrad, K., Müller, R. D., Romanowicz, B.,
 671 Steinberger, B. and Whittaker, J. M.: Mantle plumes and their role in Earth processes, *Nat. Rev.*
 672 *Earth Environ.*, 2(6), 382–401, doi:10.1038/s43017-021-00168-6, 2021.

673 Lénat, J. F., Merle, O. and Lespagnol, L.: La réunion: An example of channeled hot spot plume, *J.*
 674 *Volcanol. Geotherm. Res.*, 184(1–2), 1–13, doi:10.1016/j.jvolgeores.2008.12.001, 2009.

675 Maia, M., Pessanha, I., Courrges, E., Patriat, M., Gente, P., Hémond, C., Janin, M., Johnson, K.,
 676 Roest, W., Royer, J. Y. and Vatteville, J.: Building of the Amsterdam-Saint Paul plateau: A 10 Myr
 677 history of a ridge-hot spot interaction and variations in the strength of the hot spot source, *J. Geophys.*
 678 *Res. Solid Earth*, 116(9), 1–19, doi:10.1029/2010JB007768, 2011.

679 Mittelstaedt, E., Ito, G. and Behn, M. D.: Mid-ocean ridge jumps associated with hotspot magmatism,

680 Earth Planet. Sci. Lett., 266(3–4), 256–270, doi:10.1016/j.epsl.2007.10.055, 2008.

681 Mittelstaedt, E., Ito, G. and Van Hunen, J.: Repeat ridge jumps associated with plume-ridge
682 interaction, melt transport, and ridge migration, *J. Geophys. Res. Solid Earth*, 116(1), 1–20,
683 doi:10.1029/2010JB007504, 2011.

684 Mittelstaedt, E., Soule, S., Harpp, K., Fornari, D., McKee, C., Tivey, M., Geist, D., Kurz, M. D.,
685 Sinton, C. and Mello, C.: Multiple expressions of plume-ridge interaction in the Galápagos: Volcanic
686 lineaments and ridge jumps, *Geochemistry, Geophys. Geosystems*, 13(5),
687 doi:10.1029/2012GC004093, 2012.

688 Montelli, R., Nolet, G., Dahlen, F. A., Masters, G., Engdahl, E. R. and Hung, S. H.: Supporting
689 OnlineMaterial Timing, *Science*, 303(5656), 338–343, doi:10.1126/science.1092485, 2004.

690 Morgan, W. J.: Rodriguez, Darwin, Amsterdam, ..., A second type of Hotspot Island, *J. Geophys.*
691 *Res. Solid Earth*, 83(8), 5355–5360, 1978.

692 Müller, R. D., Roest, W. R. and Royer, J.-Y.: Asymmetric sea-floor spreading caused by
693 ridge–plume interactions, *Nature*, 396(6710), 455–459, doi:10.1038/24850, 1998.

694 Müller, R. D., Seton, M., Zahirovic, S., Williams, S. E., Matthews, K. J., Wright, N. M., Shephard, G.
695 E., Maloney, K. T., Barnett-Moore, N., Hosseinpour, M., Bower, D. J. and Cannon, J.: Ocean Basin
696 Evolution and Global-Scale Plate Reorganization Events since Pangea Breakup, *Annu. Rev. Earth*
697 *Planet. Sci.*, 44, 107–138, doi:10.1146/annurev-earth-060115-012211, 2016.

698 Niu, Y.: Ridge suction drives plume-ridge interactions, , (October), doi:10.13140/2.1.4728.0961,
699 2014.

700 O’Connor, J. M., Jokat, W., Le Roex, A. P., Class, C., Wijbrans, J. R., Keßling, S., Kuiper, K. F. and
701 Nebel, O.: Hotspot trails in the South Atlantic controlled by plume and plate tectonic processes, *Nat.*

702 Geosci., 5(10), 735–738, doi:10.1038/ngeo1583, 2012.

703 Ranalli: Rheology of the Earth, 1995.

704 Ribe, N. M.: The dynamics of plume-ridge interaction: 2. Off-ridge plumes, , 101, 1996.

705 Ribe, N. M. and Christensen, U. R.: Three-dimensional modeling of plume-lithosphere interaction, ,
706 99, 669–682, 1994.

707 Ribe, N. M. and Christensen, U. R.: The dynamical origin of Hawaiian volcanism, Earth Planet. Sci.
708 Lett., 171(4), 517–531, doi:10.1016/S0012-821X(99)00179-X, 1999.

709 Ribe, N. M., Christensen, U. R. and Theißing, J.: The dynamics of plume-ridge interaction, 1:
710 Ridge-centered plumes, Earth Planet. Sci. Lett., 134(1–2), 155–168,
711 doi:10.1016/0012-821X(95)00116-T, 1995.

712 Rowley, D. B. and Forte, A. M.: Kinematics of the East Pacific Rise Retrodicted From Pacific and
713 Farallon/Nazca Subduction-Related Torques: Support for Significant Deep Mantle Buoyancy
714 Controlling EPR Spreading, J. Geophys. Res. Solid Earth, 127(2), 1–24, doi:10.1029/2020JB021638,
715 2022.

716 Rowley, D. B., Forte, A. M., Rowan, C. J., Glišović, P., Moucha, R., Grand, S. P. and Simmons, N.
717 A.: Kinematics and dynamics of the east pacific rise linked to a stable, deep-mantle upwelling, Sci.
718 Adv., 2(12), 1–19, doi:10.1126/sciadv.1601107, 2016.

719 Rychert, C. A., Harmon, N., Constable, S. and Wang, S.: The Nature of the
720 Lithosphere-Asthenosphere Boundary, J. Geophys. Res. Solid Earth, 125(10), 1–39,
721 doi:10.1029/2018JB016463, 2020.

722 Schilling, J. G.: Fluxes and excess temperatures of mantle plumes inferred from their interaction with
723 migrating mid-ocean ridges, Nature, 352(6334), 397–403, doi:10.1038/352397a0, 1991.

724 Sleep, N. H.: Lateral flow and ponding of starting plume material, *J. Geophys. Res. Solid Earth*,
725 102(B5), 10001–10012, doi:10.1029/97jb00551, 1997.

726 Small, C.: Observations of ridge-hotspot interactions in the Southern Ocean, *J. Geophys. Res.*,
727 100(B9), doi:10.1029/95jb01377, 1995.

728 Straume, E. O., Gaina, C., Medvedev, S., Hochmuth, K., Gohl, K., Whittaker, J. M., Abdul Fattah, R.,
729 Doornenbal, J. C. and Hopper, J. R.: GlobSed: Updated Total Sediment Thickness in the World's
730 Oceans, *Geochemistry, Geophys. Geosystems*, 20(4), 1756–1772, doi:10.1029/2018GC008115,
731 2019.

732 Toomey, D. R., Wilcock, W. S. D., Conder, J. A., Forsyth, D. W., Blundy, J. D., Parmentier, E. M.
733 and Hammond, W. C.: Asymmetric mantle dynamics in the MELT region of the East Pacific Rise,
734 *Earth Planet. Sci. Lett.*, 200(3–4), 287–295, doi:10.1016/S0012-821X(02)00655-6, 2002.

735 Torsvik, T. H., Smethurst, M. A., Burke, K. and Steinberger, B.: Large igneous provinces generated
736 from the margins of the large low-velocity provinces in the deep mantle, *Geophys. J. Int.*, 167(3),
737 1447–1460, doi:10.1111/j.1365-246X.2006.03158.x, 2006.

738 Turcotte, D. and Schubert, G.: *Geodynamics*, Cambridge University Press., 2014.

739 Vlastélic, I. and Dosso, L.: Initiation of a plume-ridge interaction in the South Pacific recorded by
740 high-precision Pb isotopes along Hollister Ridge, *Geochemistry, Geophys. Geosystems*, 6(5), 1–13,
741 doi:10.1029/2004GC000902, 2005.

742 Whittaker, J. M., Afonso, J. C., Masterton, S., Müller, R. D., Wessel, P., Williams, S. E. and Seton,
743 M.: Long-term interaction between mid-ocean ridges and mantle plumes, *Nat. Geosci.*, 8(6),
744 doi:10.1038/NGEO2437, 2015.

745 Wolfe, C. J., Solomon, S. C., Laske, G., Collins, J. A., Detrick, R. S., Orcutt, J. A., Bercovici, D. and

746 Hauri, E. H.: Mantle shear-wave velocity structure beneath the Hawaiian hot spot, *Science* (80-.),
747 326(5958), 1388–1390, doi:10.1126/science.1180165, 2009.

748 Yang, A. Y., Zhao, T. P., Zhou, M. F. and Deng, X. G.: Isotopically enriched N-MORB: A new
749 geochemical signature of off-axis plume-ridge interaction—A case study at 50°28'E, Southwest
750 Indian Ridge, *J. Geophys. Res. Solid Earth*, 122(1), 191–213, doi:10.1002/2016JB013284, 2017.

751

752